

Imaging of the oxygen distribution in an isothermal turbulent free jet using two-color toluene LIF imaging

K. Mohri · M. Luong · G. Vanhove · T. Dreier · C. Schulz

Received: 7 May 2010 / Revised version: 2 March 2011 / Published online: 15 May 2011
© Springer-Verlag 2011

Abstract The results of a novel technique for the quantification of oxygen in an isothermal turbulent free jet using toluene laser induced fluorescence (LIF) are presented. This method relies on the red-shift of the toluene LIF emission spectrum with increasing oxygen concentration. Evaluating the LIF signal ratio from two different wavelength regions simultaneously produces results that depend only on the local oxygen concentration. From calibration data, obtained from repeated tests, the oxygen sensitivity of the two-color LIF technique is best for oxygen partial pressures $p_{O_2} \leq 120$ mbar in the current setup. Quantified images of oxygen distribution are presented for 40.4, 60.5, 80.5, and 103 mbar p_{O_2} in the toluene-seeded jet flow that is shielded by a toluene-seeded nitrogen co-flow at atmospheric pressure and temperature. Based on the average oxygen concentration images (obtained from 100 instantaneous oxygen images), the error in accuracy of measuring the oxygen concentration was 0.8, 3.0, 7.7, and 7.3% with a precision of $\pm 8.6, 5.5, 13.3,$ and 11.6% for the jet $p_{O_2} = 40.4, 60.5, 80.5,$ and 103 mbar cases, respectively. The main jet flow characteristics have been captured by the technique as determined from the measured oxygen distribution images. Centerline profiles of average oxygen concentration, normalized to the value at the nozzle exit, demonstrate self-similar behavior

from 5 mm above the nozzle exit. Radial oxygen concentration profiles exhibit a Gaussian-type distribution that broadens with distance above the nozzle exit, in agreement with literature.

1 Introduction

Quantifying the instantaneous distribution of oxygen is highly desirable in various applications. For instance, the determination of the proper fuel/air ratio in flames and internal combustion engine operation has been a vital aspect in the optimization of practical combustion processes. The demand for lower emission and higher efficiency combustion processes has been the motivation for research toward more extensive understanding of engine operation using laser based in-situ diagnostics strategies [1]. Determining the conditions of the fuel/air mixture in terms of fuel concentration, oxygen concentration and temperature plays a pivotal role since it has a critical impact on the ignition behavior and on subsequent combustion. While qualitative measurements of fuel density are feasible based on the fluorescence properties of commercial fuels [2] a quantitative determination of fuel concentrations is often based on the use of well characterized fluorescent tracers [3]. The fluorescence intensity of these tracers often depends not only on the tracer concentration but also on temperature, total pressure and oxygen partial pressure. While the dependence on total pressure is generally weak, the dependence on oxygen partial pressure is particularly strong with aromatic compounds. Based on this cross-influence of temperature and oxygen partial pressure on the LIF signal, it is possible to determine these additional quantities from the signal evaluation. In situations where the concentration of the fluorescent

K. Mohri (✉) · M. Luong · T. Dreier · C. Schulz
IVG, University of Duisburg-Essen, Duisburg, Germany
e-mail: khadijeh.mohri@uni-due.de

C. Schulz
CeNIDE, Center for Nanointegration Duisburg-Essen, Duisburg,
Germany

G. Vanhove
PC2A, UMR 8522 CNRS Universite de Lille 1, Villeneuve
d'Ascq, France

tracer does not change, the variation in total signal can be directly interpreted as a measure of temperature [4, 5] or oxygen partial pressure. In situations, where the concentration varies, two-color measurements have been used to derive T or p_{O_2} information from a ratio of two signals that then is independent of the local tracer concentration (e.g. [6]).

For the measurement of fuel/air ratios a variety of different approaches have been presented. Previous investigations have used instantaneous temperature distribution information in the compression stroke and the unburned end-gas of a spark ignition engine in order to calculate the fuel/air equivalence ratio assuming constant oxygen content in the intake air, as presented by Einecke et al. [6]. A similar approach was used by Rothamer et al. [7]. The technique requires simultaneous excitation with two different laser wavelengths, for example at 248 and 308 nm and is therefore experimentally challenging. The FARLIF approach suggested by Reboux [8] takes advantage of the strong quenching of toluene LIF by oxygen in order to directly measure the fuel/air equivalence ratio. Although this method works well at low temperatures it does not give any information about absolute concentrations. Furthermore, its extensions to engine conditions become questionable at high temperatures as shown by Koban et al. [9]. For measurement of oxygen concentrations in fuel/air mixtures, Koban et al. used the different responses of toluene and 3-pentanone to collisional quenching by molecular oxygen in their two-tracer technique [10]. Their experiments were conducted at room temperature and atmospheric pressure. An application to internal combustion engines was presented by Frieden et al. [11]. The two-tracer approach, however, is based on the assumption that the concentration ratio of both tracers is not varying. Additionally, non-radiative energy transfer between the tracers must be accounted for [10]. Toluene was suggested for a simplified method with single-line excitation and two-line detection for measuring temperature [5] that could in a similar way also be used for measuring the oxygen concentration. The experimental demonstration for this technique, however, was missing so far and is presented in this paper.

As a second field of application the imaging of oxygen distribution, based on the method described in this paper, can be used as a tool to determine the level of mixing within the flow and to distinguish between macroscopic mixing (stirring) and mixing on a molecular level (micro mixing). It has been shown that quantitative images of molecular mixing in free shear flows may be obtained using tracer species. LIF images of nitric oxide and acetone have been used by King et al. [12] and Meyer et al. [13]. King et al. investigated the extent to which an axisymmetric shear layer, in the form of a jet, is mixed at the molecular level while Meyer et al. have studied the role of large- and intermediate-scale structures in determining the state of molecular mixing in the developing and far-field regions of gaseous planar

shear layers. Yip et al. [14] have visualized gas-phase fluid mixing processes using the technique of sensitized phosphorescence from acetone/biacetyl and toluene/biacetyl systems. Because quenching of aromatic tracers occurs predominantly upon collision with oxygen molecules, the effects of quenching that are described later in this paper would only be present in case of micro-mixed gases.

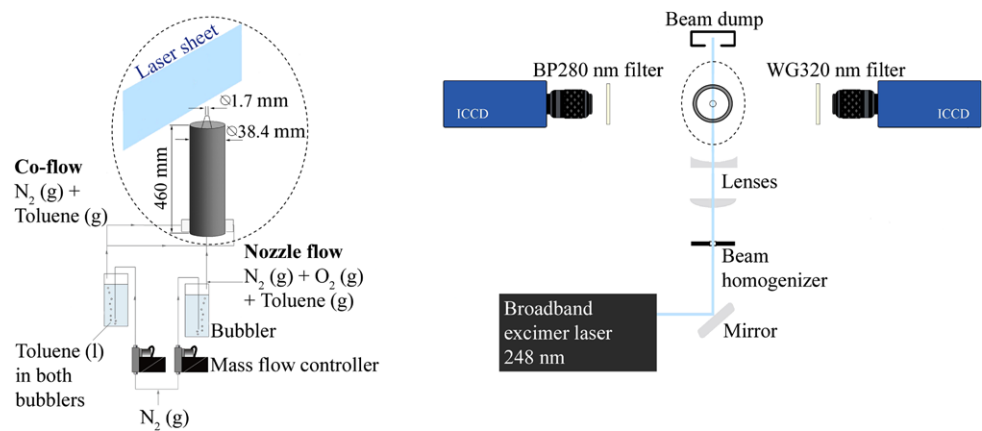
Quantitative imaging diagnostics which are based on tracers require a detailed knowledge about the spectroscopic characteristics of the relevant fluorescent tracers. The strong dependence of toluene LIF on oxygen and the available photophysical studies on toluene [9, 15] makes this tracer attractive for measuring local oxygen concentrations. In the present work results of experiments aimed at quantifying the distribution of oxygen, by detecting the effect of quenching on the emission spectra, are presented.

2 Experimental

The experimental setup, depicted in Fig. 1, consists of a conical nozzle (exit diameter $d = 1.7$ mm, length $l = 222.3$ mm). The first 197 mm of the nozzle is cylindrical in shape with a constant diameter of 8 mm and the conical end, of length 25.4 mm, has a half-angle of 9° . The nozzle is mounted co-axially within a 38.4 mm diameter aluminum tube that is 460 mm long and delivers a low velocity outer co-flow ($U_\infty = 0.52$ m/s). The tip of the nozzle extrudes out of the co-flow tube by 2 mm. The jet flow Reynolds number ranges between $Re_d = U_e d/\nu = 1914$ and $Re_d = U_e d/\nu = 2113$, for the $p_{O_2} = 0$ and 103 mbar cases, respectively, where U_e and d are the nozzle exit velocity and exit diameter, respectively, and $\nu = \mu/\rho$ is the kinematic viscosity of the gas mixtures. The tests were carried out at room temperature and pressure, maintaining isothermal conditions to avoid simultaneous effects of temperature variation on the toluene LIF spectrum. A bubbler system was used to seed the gases with toluene in both the jet flow (0.3% by volume toluene) and co-flow (0.01% toluene) providing LIF signal throughout the entire region of interest. The percentage of toluene within the flows was confirmed through gas chromatography tests. A lower amount of toluene was used in the co-flow to minimize attenuation of the excitation laser light by the tracer [16]. Controlled amounts of oxygen could be introduced into the jet flow and/or co-flow. All gas flows were metered using appropriate mass flow controllers (MKS and Tylan) which were calibrated for each specific gas.

A light sheet generated by a krypton fluoride (KrF) excimer laser (Lambda Physik, LPX 120) with a beam at 248 nm (20 ns pulse width, broadband output at 1 Hz repetition rate) was used to excite the toluene. The laser sheet fluence chosen was 20.8 mJ/cm², thus taking precautions that

Fig. 1 Experimental setup: Toluene-seeded jet flow ($N_2 + O_2$) shielded by a toluene-seeded N_2 co-flow (left panel). Excitation is achieved by a KrF excimer laser sheet. Toluene LIF is detected simultaneously by two cameras in two different wavelength regions of the spectrum (right panel)



the LIF signal vs. laser energy remains linear [17]. The laser sheet was homogenized with the aid of a beam homogenizer (SUSS MicroOptics) that is placed before the sheet-forming optics (cf. Fig. 1). Two intensified CCD cameras (Lavision, Flamestar2 and Nanostar, respectively) each fitted with a UV lens ($f = 105$ mm, $f_{\#} = 4.5$ and $f = 100$ mm, $f_{\#} = 2.8$, respectively) were located on opposite sides of the jet to capture the fluorescence at 90° to the laser sheet plane. The cameras were synchronized with the laser trigger to record the LIF images simultaneously at a rate of 1 Hz. Appropriate filters were used to capture the shorter and longer wavelength regions of the emission spectrum (a band pass Semrock BP280 filter, and a long pass Schott WG320 filter, respectively). Measurements showed that the interference band pass BP280 filter detects the peak toluene fluorescence at $\lambda = 280 \pm 14$ nm, and the WG320 filter detects the wavelength region $\lambda \geq 320$ nm. The DaVis software from LaVision was utilized for data acquisition and processing.

3 Theoretical background

Consequential to UV excitation, the emitted LIF signal S of a tracer, such as toluene as in our case [3, 18], depends on the laser intensity I_{laser} , the detection volume V , the tracer number density n and its absorption cross section σ , the detection efficiency η and fluorescence quantum yield $\Phi(n_q)$ of the tracer which is a function of the number density, n_q , of any quenching species that are present, in the present case oxygen.

$$S \propto I_{\text{laser}} V n \sigma \eta \Phi(n_q) \quad (1)$$

The fluorescence quantum yield Φ is interpreted as the ratio of the rate of fluorescence k^{fl} to the sum of all de-excitation rates. These include the intramolecular rates ($k^{\text{non-rad}}$ for the non-radiative pathways and k^{fl} for the fluorescing pathway), and the intermolecular collisional quench-

ing rate k^q :

$$\phi = \frac{k^{fl}}{k^{\text{non-rad}} + k^{fl} + k^q n_q} \quad (2)$$

Often the Stern–Volmer plot, that is the inverse of the fluorescence signal normalized by the unquenched signal, S_0 , versus the quencher concentration, is evaluated in order to obtain a measure of the quenching rate. The slope of the Stern–Volmer plot $k_{SV} = \frac{k^q}{k^{\text{non-rad}} + k^{fl}}$, which represents the effect of quenching relative to the total intramolecular de-excitation rate, would indicate the strength of quenching [3]. In our case for the longer and shorter wavelength parts of the spectrally integrated signal intensities (selected by the Schott filters BP280 and WG320, respectively) the Stern–Volmer expressions are

$$S^{\text{WG320}} = \frac{S_0^{\text{WG320}}}{1 + k_{SV}^{\text{WG320}}[\text{O}_2]}$$

and

$$S^{\text{BP280}} = \frac{S_0^{\text{BP280}}}{1 + k_{SV}^{\text{BP280}}[\text{O}_2]} \quad (3)$$

where S^{WG320} or S^{BP280} are signal intensities with O_2 in flow, S_0^{WG320} or S_0^{BP280} are signal intensities without O_2 in flow, and K_{SV}^{WG320} or K_{SV}^{BP280} are the Stern–Volmer constants.

The normalized signal ratios are then:

$$S_R = \frac{S^{\text{WG320}}}{S^{\text{BP280}}} = \left(\frac{1 + k_{SV}^{\text{BP280}}[\text{O}_2]}{1 + k_{SV}^{\text{WG320}}[\text{O}_2]} \right) \left(\frac{S_0^{\text{WG320}}}{S_0^{\text{BP280}}} \right) \quad (4)$$

The oxygen concentration $[\text{O}_2]$ can therefore be calculated via (5)

$$[\text{O}_2] = \frac{S_{R0} - S_R}{S_R K_{SV}^{\text{WG320}} - S_{R0} K_{SV}^{\text{BP280}}} \quad (5)$$

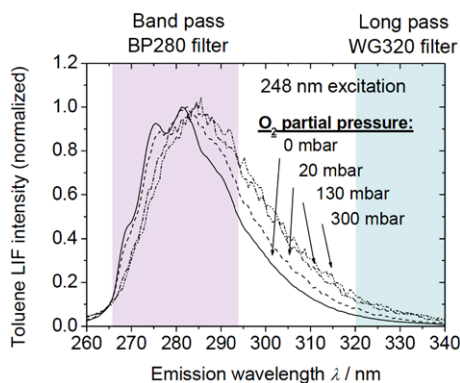


Fig. 2 Red-shift of the toluene LIF emission with increasing O_2 partial pressure with 248 nm excitation at room temperature (adapted from [15])

where $S_{R0} = \frac{S_0^{WG320}}{S_0^{BP280}}$.

If calibration data are obtained with the same setup as the desired measurements, $[O_2]$ can then be directly determined from a calibration curve without calculating the K_{SV} values first.

Quenching of the fluorescence from aromatic molecules in the presence of oxygen is a well-known phenomenon [19, 20]. Almost every collision with oxygen leads directly to electronic de-activation [15]. On the other hand collisions with nitrogen are not likely to change the electronic state. Therefore, it is a reasonable approximation to regard oxygen as the only important colliding species that influences the signal intensity. It has been shown experimentally that with 248 nm excitation of toluene at room temperature and air pressures above 3 bar, oxygen quenching is the dominant de-excitation pathway and intramolecular relaxation can be neglected [8].

The long wavelength part of the toluene LIF spectrum is affected less by oxygen quenching than the region around the 280 nm peak, thus indicating a similar red-shift effect that has also been shown for the temperature dependent cases presented in the past [5]. This phenomenon, shown for excitation of toluene at 248 nm at room temperature in Fig. 2, is limited to relatively low oxygen partial pressures. Above ~ 200 mbar O_2 , no significant change in the spectrum has been observed with further increasing oxygen partial pressures [15]. The local toluene and oxygen concentrations vary simultaneously where the jet flow mixes inhomogeneously with the surrounding co-flow. Forming the ratio of two simultaneously recorded LIF signals from two different wavelength regions will cancel out the tracer concentration and the local laser fluence and the result in principle provides quantitative information about the local oxygen content. To simplify the determination of the relative response of both detectors, however, a calibration measurement at a known oxygen concentration is performed. The influence of signal trapping, from the long wavelength end

of the toluene absorption spectrum, in the BP280 detection channel has been analyzed using spectrally-resolved absorption cross section measurements [21]. Assuming a worst case scenario where the maximum concentration of toluene, the value at the center of the jet close to the nozzle exit, covers a path length of 40 mm (diameter of co-flow cylinder is 38.4 cm) showed the fractional re-absorption of fluorescence radiation to be less than 0.5%. Therefore, the effect of signal trapping is considered negligible.

4 Data processing

Each set of two instantaneous LIF images obtained simultaneously from opposite sides of the jet and co-flow are first corrected for background signal that has been recorded with the laser on but without flow. Because ratios of images are used in the following analysis only, a correction for the laser sheet intensity variation and laser pulse energy are not necessary as long as the laser fluence does not exceed the range of linear signal response. The two images are then corrected for distortions and one image is flipped and matched onto the other with sub-pixel resolution. For the image matching step an adequately designed grid (1 mm diameter dots distanced by 2 mm from each other) that is printed on transparent film is placed in the location of the laser sheet and its image is captured using both cameras. For consistency this grid image is obtained before and after each test. The DaVis software (Lavisision) uses the grid images from each camera to calculate the required image distortion corrections. A further improvement of the image matching may be made by using image pairs of tracer signal rather than images of the reference pattern only, as shown by Tea et al. [22].

The corrected images are numerically filtered using a spatial averaging filter. Various filter box sizes were investigated and a 5×5 pixel ($0.36 \times 0.36 \text{ mm}^2$) box size was chosen. The projected pixel size in the images is 0.07 mm/pixel and it is assumed that the chosen filter box size does not significantly deteriorate the spatial resolution that is limited by the image intensifier. The simultaneous images, from the short and long wavelength regions of the LIF spectrum, are then divided with each other and normalized by the reference intensity ratio (from experiments without O_2 obtained for each camera) in accordance with (4). The result provides the normalized ratio of signals from the two wavelength regions detected. In order to obtain the oxygen concentrations for each divided image set, the appropriate calibration curve obtained using the same filter combination is applied (cf. Fig. 4). Figure 3 shows an example of an O_2 image that is obtained from two instantaneous LIF images for the case with seeding of 60.5 mbar O_2 into the jet flow.

Fig. 3 Illustration of the two-color toluene LIF technique applied to obtain a quantitative distribution of the O_2 concentration for 60.5 mbar O_2 in the jet flow. Shown are instantaneous LIF images and the resulting oxygen distribution

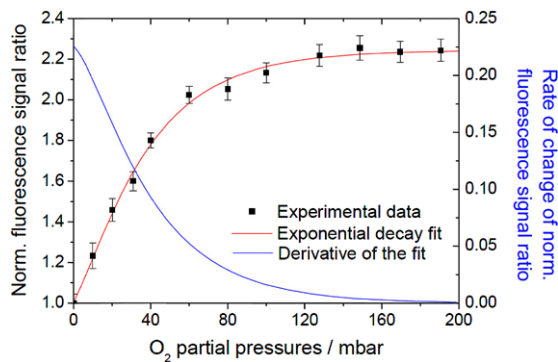
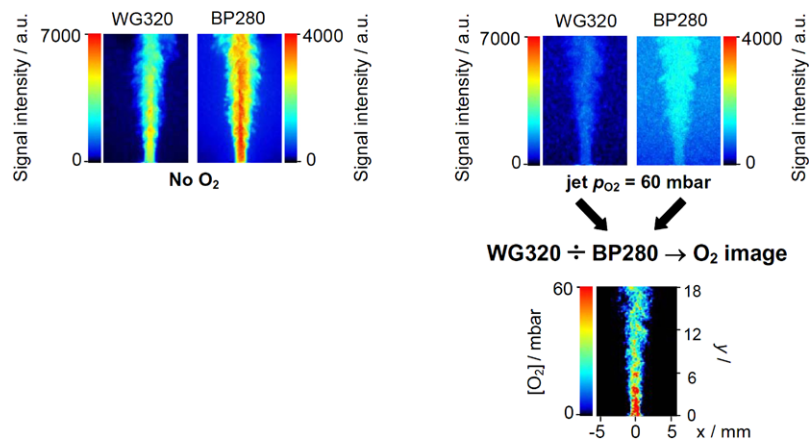


Fig. 4 Calibration curve of the normalized LIF signal ratio (for the BP280–WG320 filter pair) against O_2 partial pressures

5 Results and discussion

5.1 Choice of detection filters

Various combinations of detection wavelength ranges were investigated using appropriate pairs of Schott filters for the two cameras. These were: BP280–WG320, BP280–WG305, and WG280–WG305 (BP280 is a bandpass filter centered at 280 nm and WG305 and WG320 are long pass filters with cut-off wavelengths of 305 and 320 nm, respectively). For the determinations of calibration curves, data were obtained from a region with a size of 190×190 pixels or 13.3×13.3 mm², with homogeneous and controlled oxygen concentrations. This reference condition was generated by adding various concentrations of toluene and oxygen to the co-flow and running the experiment without the central jet flow. The BP280–WG320 filter pair provided the strongest signals and the best sensitivity to oxygen concentration and hence this combination was used in all the measurements presented here.

The calibration curve (signal ratio vs. oxygen partial pressure) obtained for this filter combination, which has been used to obtain the final $[O_2]$ images presented is shown in Fig. 4. The error bars, shown in absolute values on the

graph, are determined from the variation of signal ratios from several independent measurements using the configuration and spatial resolution mentioned above. On the same graph the rate of change of the normalized fluorescence signal against oxygen partial pressures is plotted. From this it can be argued that for the current conditions the technique works up to approximately $p_{O_2} \sim 120$ mbar O_2 . Above ~ 140 mbar O_2 the signal ratio becomes almost independent of variations in oxygen partial pressure resulting in poor sensitivity.

The signal in both detection channels shows an almost hyperbolic dependence on the oxygen pressure. Due to the resulting strong non-linearity of the LIF signals with varying oxygen concentrations, it is mathematically necessary to calculate the oxygen maps from instantaneous (as opposed to averaged) LIF images. However, because ratioing instantaneous images with limited signal-to-noise level leads to a significant increase in noise, in cases where S/N-ratios are low, averaging of the measurements on each channel before calculating the ratio might lead to overall higher quality results. In the present paper, all averaged O_2 concentration images presented have been obtained from 100 instantaneous O_2 concentration maps that are calculated using instantaneous LIF images.

5.2 Signal sensitivity

One of the challenges in the current technique is the measurement of low signal levels and the resulting restrictions in signal-to-noise ratios. Quenching reduces the signal intensity dramatically and therefore, the initial signal intensity in the no-oxygen case should be high enough in order to achieve measurable intensities when oxygen is added to the flow. In Fig. 5 the toluene LIF images (averaged from 100 instantaneous images) of the jet flow with no oxygen and with 80.5 mbar O_2 are shown for the long wavelength, i.e., intrinsically weaker, detection channel ($\lambda \geq 320$ nm). For the conditions used, the average signal intensity within the

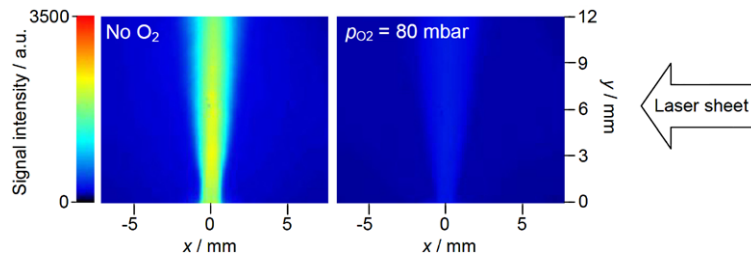


Fig. 5 Averaged toluene LIF images obtained using the WG320 filter for the jet flow containing no O₂ (left), and 80.5 mbar O₂ in the center flow (right). Co-flow: N₂ seeded with toluene

Table 1 Signal levels, S , relative to the no-oxygen signal, S_0 , from each detection channel obtained from a region close to the nozzle exit and the corresponding signal-to-noise ratios, S/N , for each detection channel. The error in accuracy of measuring the oxygen concentration, ε , and a statistical average of precision in the [O₂], σ , are also shown. The error in accuracy and precision are determined from the same region of interest in the averaged O₂ images that are obtained using 100 instantaneous O₂ images

p_{O_2}/mbar	$\frac{S_{BP280}}{S_0}$	S/N^{BP280}	$\frac{S_{WG320}}{S_0}$	S/N^{WG320}	ε	σ
0	1.00	29.2	1.00	24.8	–	–
40.4	0.08	19.4	0.13	19.8	0.8%	$\pm 8.6\%$
60.5	0.06	18.4	0.10	19.5	3.0%	$\pm 5.5\%$
80.5	0.05	18.5	0.09	19.2	7.7%	$\pm 13.3\%$
103	0.04	18.1	0.08	18.2	7.3%	$\pm 11.6\%$

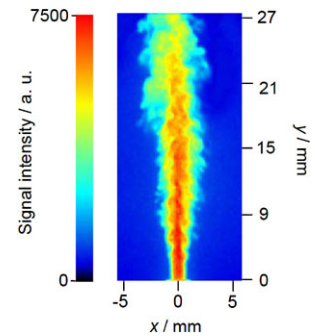
jet center flow near the nozzle (obtained from a box of size 9×11 pixels) went down by a factor of approximately 11 when 80.5 mbar O₂ was added to the jet flow. The signal-to-noise ratio, S/N , for each detection channel is determined from a homogeneous region close to the nozzle exit for each jet p_{O_2} case. The results are given in Table 1. The data show a decrease in S/N for both detection channels with increasing jet p_{O_2} . In both detection channels the S/N is severely reduced in the presence of oxygen addition to the jet flow.

The initial signal intensities could be enhanced through various measures e.g. increasing the laser energy, increasing the concentration of toluene within the flow or improving the solid angle of detection and the filter transmission. However, it is essential that all the contributing parameters are optimized for the specific setup and conditions if it is desired to maintain a linear signal response and to avoid laser attenuation effects, and to keep the required large dynamic range and good signal-to-noise levels.

5.3 Oxygen concentration imaging measurements

To better understand the O₂ concentration images presented, it is useful to have a brief look at the jet flow structure. For this purpose, an instantaneous LIF image (taken from the stronger detection channel using the BP280 filter) is shown for the oxygen-free case in Fig. 6. The vortical structures

Fig. 6 Instantaneous LIF image of the oxygen-free jet flow, obtained from the stronger detection channel (BP280 filter)



seen close to the nozzle exit, at the jet/co-flow interface, resemble the ring-like structures in the heated air jet emerging from the smooth contraction nozzle of Mi et al. [23], although their flow had a much higher Reynolds number, $Re_d = 16,000$. Several researchers have analyzed the flow structure of various jets. The formation of relatively large structures, as seen in Fig. 6, is often attributed to a laminar state of the shear layer, while small-scale structures are seen to indicate the presence of turbulence [23]. The shear layer is formed due to the velocity gradient between the jet and co-flow ($U_e/U_\infty = 33$ for the case shown in Fig. 6). The growth of instabilities can lead to a roll-up of the shear layer as seen in close proximity of the nozzle exit. In Fig. 6 it can be seen that the ring-like vortical structures close to the nozzle exit appear to break up further downstream indicating an increased level of turbulence. The higher level of turbulence increases the entrainment of the surrounding co-flow into the jet and would enhance the mixing process between the two flows. This is reflected in the [O₂] images shown in Fig. 7 as discussed below.

Examples of instantaneous and averaged oxygen concentration fields obtained for four jet p_{O_2} cases (40.4, 60.5, 80.5 and 103 mbar), are presented in Fig. 7. The [O₂] images in Fig. 7 illustrate that, as expected, the maximum O₂ concentration is present mainly near the nozzle exit before the jet flow begins to mix with the outer coflow. As the flow spreads out further downstream of the axisymmetric nozzle, the oxygen concentration would be expected to reduce in the center plane of the jet flow (where the laser sheet is located). The O₂ concentrations close to the jet exit, where we

Fig. 7 O_2 concentration fields for jet $p_{O_2} = 40.4, 60.5, 80.5$ and 103 mbar

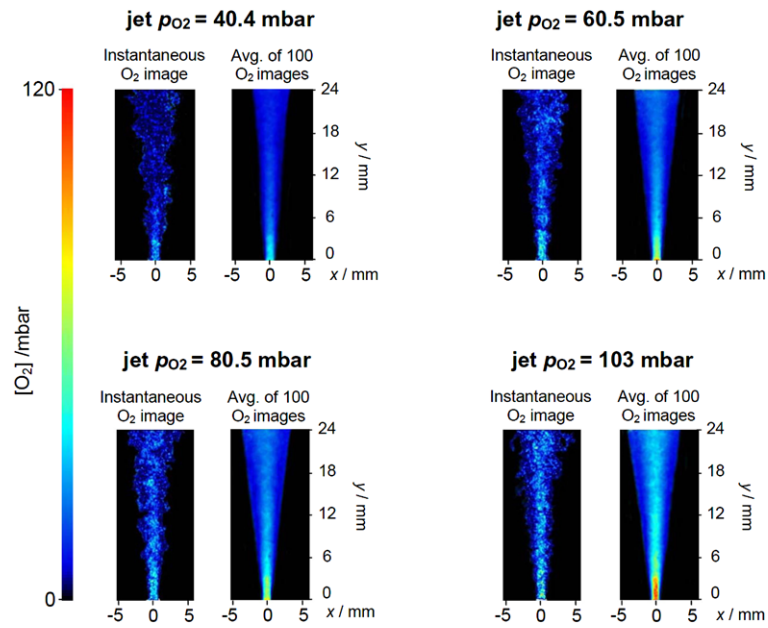
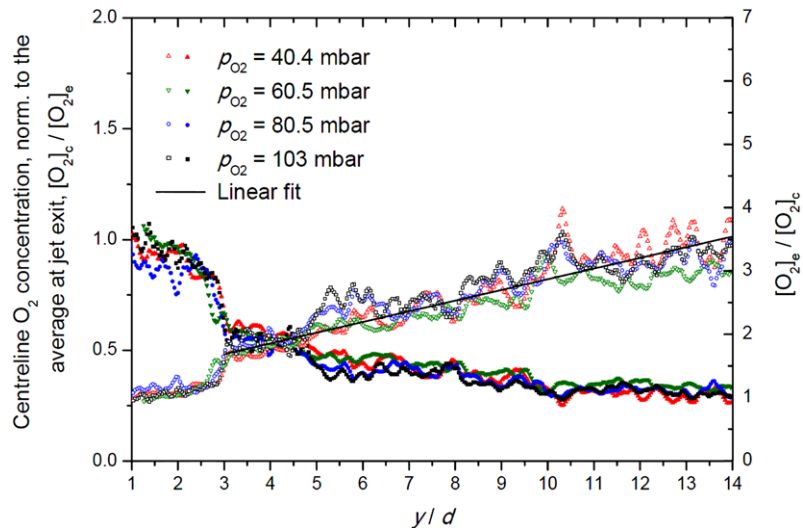


Fig. 8 Averaged O_2 -concentration along the centerline, normalized to the values at the nozzle exit, $[O_2]/[O_2]_e$, filled symbols. Reciprocal data ($[O_2]_e/[O_2]$) are shown as *open symbols* with a linear fit



expect a homogeneous region prior to onset of mixing with the co-flow, are compared to p_{O_2} . In the ideal case the two values should be similar within the potential core of the jet. The values were found to differ by 0.8, 3.0, 7.7, and 7.3% for the jet $p_{O_2} = 40.4, 60.5, 80.5,$ and 103 mbar cases, respectively. The data were evaluated within a rectangular region of 9×11 pixels (corresponding to $0.64 \times 0.79 \text{ mm}^2$) along the jet center using the average of 100 instantaneous O_2 images in each case. By assessing the variation of the O_2 concentration within the same area of interest close to the nozzle exit in the averaged O_2 images, the corresponding precision in O_2 measurement is found to be $\pm 8.6, 5.5, 13.3,$ and 11.6% for the jet $p_{O_2} = 40.4, 60.5, 80.5,$ and 103 mbar cases, respectively.

The average oxygen concentration along the centerline was normalized to the average at the jet exit $[O_2]_e$ (Fig. 8).

This produces results with a similar axial jet flow development for all the jet p_{O_2} cases. Shown on the same graph is the reciprocal of the normalized concentration, $[O_2]_e/[O_2]$. These profiles exhibit the linear variation required for self-similarity (or self-preservation) [24] in the region $y/d \geq 3$ or $y \geq 5 \text{ mm}$. Different authors indicate various locations for the onset of the self-similarity region in their jet flows. For example, Lubbers et al. indicate the onset around $11d$ [25], Boguslawski et al. at $8d$ [26] and Adair et al. at $10d$ for a methane jet [27]. In the current experiments we expect to see self-similarity since the ratio of the co-flow to jet velocity, U_∞/U_e , for all jet p_{O_2} cases is below 5% [23]. For the minimum and maximum jet exit velocities $U_\infty/U_e = 3$ and 2.8% respectively. The conventional idea of self-similarity indicates that the flow becomes asymptotically independent of the initial conditions at some far-field distance. The onset

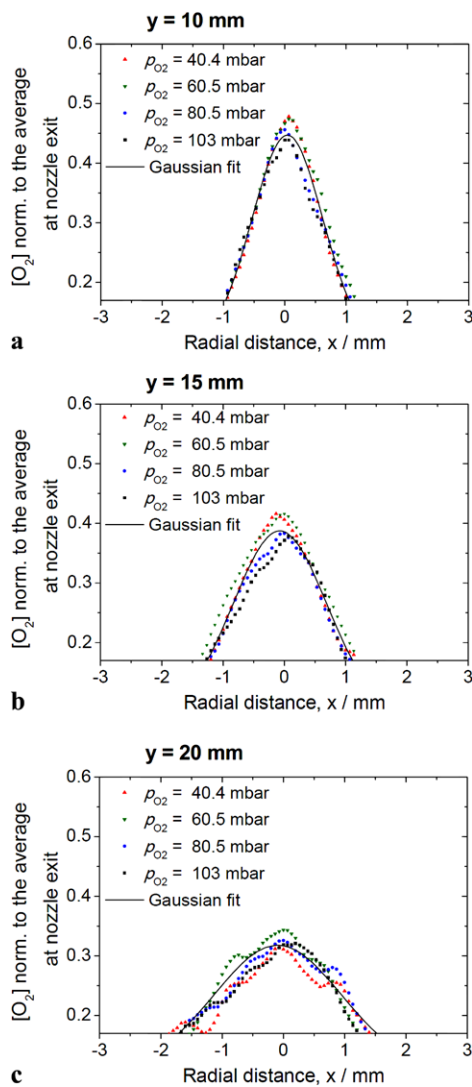


Fig. 9 Radial O_2 -concentration profiles from average $[O_2]$ images, normalized to the average in the jet center close to the nozzle exit, for various heights above the nozzle exit

of self-similarity would differ for different jet flows since the initial conditions can play a big role in the internal adjustments that a flow experiences before showing self-similar behavior. The decay of normalized mean centerline concentration may be described by the following hyperbolic relation [28]:

$$\frac{[O_2]}{[O_2]_e} = \frac{kd}{y + y_o} \quad (6)$$

The decay constant, k , and the virtual origin, y_o , are determined from experimental data by plotting the variation of $[O_2]_e/[O_2]$ with distance from the nozzle exit, which gives a slope that is equal to $1/k$ in the linear region. For the data presented in Fig. 8, linear fit formed onto the average of all reciprocals of the normalized oxygen concentration in the region $y/d \geq 3$, the decay constant and virtual origin are

found to be $k = 5.9$ and $y_o = -7d$. The value of k tends to vary between 4–6 in the literature [23, 26, 28, 29]. Interestingly, Birch et al. indicate that the value of k tends to be higher when near-field data are analyzed [29] as in our case. For their turbulent free jet, $k = 4.0$ and $y_o = -5.8d$ in the region $y/d \geq 25$ while their data at $y/d = 10$ –30 were well described using $k = 4.7$.

The corresponding radial profiles, from the average $[O_2]$ images of Fig. 7, normalized to the jet exit oxygen concentration, at fixed heights above the nozzle exit ($y = 10, 15$, and 20 mm) are shown in Fig. 9. The nozzle exit is at $y = 0$. These profiles further demonstrate that the technique has captured the expected jet flow characteristic [30–32]. With increasing height above the nozzle exit (increasing y) the profiles, which have been fitted with Gaussian-type variation, broaden and the peak value decreases.

6 Conclusions and future work

In the present work we have demonstrated absolute oxygen concentration imaging in a free turbulent isothermal jet flow, at atmospheric pressure and room temperature, using two-color toluene LIF. Oxygen concentration measurements are presented for 40.4, 60.5, 80.5, and 103 mbar O_2 in the jet flow. This has been achieved by forming a ratio from two toluene LIF signals that are obtained simultaneously from different wavelength ranges (using appropriate filters), each exhibiting a different response to oxygen quenching. The detection wavelength ranges that provided the strongest signal and sensitivity to oxygen concentration were at $\lambda = 280 \pm 14$ nm and $\lambda \geq 320$ nm. We have exploited the oxygen-dependent red-shift of the fluorescence emission resulting from the fact that the shorter wavelength region of the toluene LIF emission spectrum is more strongly affected by oxygen quenching than the longer wavelength region. The calibration data obtained, by measuring the signal ratios in regions with known O_2 concentrations show that the sensitivity of the technique is highest up to $p_{O_2} = 120$ mbar while beyond $p_{O_2} = 140$ mbar no influence of the O_2 partial pressure can be seen for the current setup. One measure of the technique's accuracy in producing $[O_2]$ maps of the jet flow has been to compare the average $[O_2]$ obtained from a region close to the nozzle exit, with the p_{O_2} in the jet. From this the error in accuracy of O_2 measurement was below 10% for all jet p_{O_2} cases, with a precision $\leq \pm 13.3\%$; see Table 1. The two-dimensional centerline and radial jet oxygen concentration profiles, from the averaged $[O_2]$ images, exhibit the main jet flow characteristics in agreement with literature.

If this technique is to be used in near-atmospheric tests, there may be a possibility to increase the oxygen sensitivity with cameras that have a higher dynamic range and are

equipped with high f-number detection optics. Another possibility is increasing signal intensities through higher laser fluences and by intentionally leaving the fully linear range of signal response. The investigation of the implications will be part of future work. As part of future work also optimization of image overlap for the LIF-image pairs that are to be ratioed should be considered. In applications where mixing on a molecular level is crucial, this technique may be taken further to study the degree of mixing on a molecular level within a specific flow field. Especially if an oxygen-free flow is mixed with oxygen and the onset of mixing does not contain very high concentrations of oxygen. This is simply due to the fact that the method relies on the molecular quenching effect of oxygen on the toluene molecules in order to measure the amount of oxygen. This will have practical applications, e.g., when distinguishing between micro- and macro mixing, e.g., in supersonic combustion processes.

Acknowledgements The authors acknowledge funding by the German Research Foundation, DFG. They also thank Gustavo Ramirez (CMT, Polytechnical University of Valencia, Spain) for his experimental contribution as a summer student at IVG.

References

1. M.C. Drake, D.C. Haworth, *Proc. Combust. Inst.* **31**, 99 (2007)
2. H. Zhao, N. Ladommatos, *Prog. Energy Combust. Sci.* **24**, 297 (1998)
3. C. Schulz, V. Sick, *Prog. Energy Combust. Sci.* **31**, 75 (2005)
4. J.E. Dec, W. Hwang, *SAE Tech. Pap. Ser.* **2**, 421 (2009)
5. M. Luong, W. Koban, C. Schulz, *J. Phys. Conf. Ser.* **45**, 133 (2006)
6. S. Einecke, C. Schulz, V. Sick, *Appl. Phys. B* **71**, 717 (2000)
7. D.A. Rothamer, J.A. Snyder, R.K. Hanson, R.R. Steeper, R.P. Fitzgerald, *Proc. Combust. Inst.* **32**, 2869 (2009)
8. J. Reboux, D. Puechberty, *SAE Tech. Pap. Ser.* 941988 (1994)
9. W. Koban, J.D. Koch, R.K. Hanson, *Appl. Phys. B* **80**, 147 (2005)
10. W. Koban, J. Schorr, C. Schulz, *Appl. Phys. B* **74**, 111 (2002)
11. D. Frieden, V. Sick, J. Gronki, C. Schulz, *Appl. Phys. B* **75**, 137 (2002)
12. F.K. King, R.P. Lucht, J.C. Dutton, *Phys. Lett.* **22**, 633 (1997)
13. T.R. Meyer, J.C. Dutton, R.P. Lucht, *J. Fluid Mech.* **558**, 179 (2006)
14. B. Yip, A. Lozano, R.K. Hanson, *Exp. Fluids* **17**, 16 (1994)
15. W. Koban, J.D. Koch, R.K. Hanson, C. Schulz, *Appl. Phys. B* **80**, 777 (2005)
16. T. Etzkorn, B. Klotz, S. Sorensen, I.V. Patroescu, I. Barnes, K.H. Becker, U. Platt, *Atmos. Environ.* **33**, 525 (1999)
17. B.R. Petersen, J.B. Ghandhi, J.D. Koch, *Appl. Phys. B* **93**, 639 (2008)
18. J.D. Koch, R.K. Hanson, *Appl. Phys. B* **76**, 319 (2003)
19. R.G. Brown, D. Phillips, *J. Chem. Soc. Faraday Trans. II* **70**, 630 (1974)
20. C.S. Burton, W.A. Noyes, *J. Chem. Phys.* **49**, 1705 (1968)
21. W. Koban, J.D. Koch, R.K. Hanson, C. Schulz, *Phys. Chem. Chem. Phys.* **6**, 2940 (2004)
22. G. Tea, G. Bruneaux, J.T. Kashdan, C. Schulz, *Proc. Combust. Inst.* **33**, 783 (2010)
23. J. Mi, D.S. Nobes, G.J. Nathan, *J. Fluid Mech.* **432**, 91 (2001)
24. C.D. Richards, W.M. Pitts, *J. Fluid Mech.* **254**, 417 (1993)
25. C.L. Lubbers, G. Brethouwer, B.J. Boersma, *Fluid Dyn. Res.* **28**, 189 (2001)
26. L. Boguslawski, C.O. Popiel, *J. Fluid Mech.* **90**, 531 (1979)
27. D. Adair, M.R. Malin, B.A. Younis, *Appl. Math. Model.* **16**, 476 (1992)
28. J.A. Hinze, *Turbulence* (McGraw-Hill, New York, 1975)
29. A.D. Birch, D.R. Brown, M.G. Godson, J.R. Thomas, *J. Fluid Mech.* **88**, 431 (1978)
30. B.H. Cheung, R.K. Hanson, *Appl. Phys. B* **98**, 581 (2010)
31. H.A. Becker, H.C. Hottel, G.C. Williams, *J. Fluid Mech.* **30**, 285 (1967)
32. C. Fukushima, L. Aanen, J. Westerweel, *Laser Techniques for Fluid Mechanics* (Springer, Berlin, 2002), p. 339